



# A new hydrous iron oxide phase stable at mid-mantle pressures

Huawei Chen<sup>a,b,\*</sup>, Sheng-Yi Xie<sup>c</sup>, Byeongkwan Ko<sup>b</sup>, Taehyun Kim<sup>d</sup>, Carole Nisr<sup>b</sup>, Vitali Prakapenka<sup>e</sup>, Eran Greenberg<sup>e</sup>, Dongzhou Zhang<sup>e</sup>, Wenli Bi<sup>f</sup>, Alp E. Ercan<sup>f</sup>, Yongjae Lee<sup>d</sup>, Sang-Heon Shim<sup>b,\*\*</sup>

<sup>a</sup> School of Earth Sciences, China University of Geosciences, Wuhan, Hubei, China

<sup>b</sup> School of Earth and Space Exploration, Arizona State University, Tempe, AZ, USA

<sup>c</sup> School of Physics and Electronics, Hunan University, Changsha, Hunan, China

<sup>d</sup> Department of Earth System Sciences, Yonsei University, Seoul, South Korea

<sup>e</sup> GeoSoilEnviroCars, University of Chicago, Chicago, IL, USA

<sup>f</sup> Advanced Photon Source, Argonne National Laboratory, Argonne, IL, USA

## ARTICLE INFO

### Article history:

Received 23 December 2019

Received in revised form 18 August 2020

Accepted 24 August 2020

Available online 3 September 2020

Editor: J. Brodholt

### Keywords:

hydrous iron oxide  
lower mantle  
crystal structure  
hydrogen

## ABSTRACT

The amount of hydrogen stored in the Earth's interior is important for a range of issues, including the volatile incorporation during the Earth formation and the co-evolution of the atmosphere, the hydrosphere, and the interior. Recent experiments found titanium bearing  $\varepsilon$ -FeOOH in a hydrous basaltic system at 12–19 GPa and 1300 K. Pyrite-type FeOOH was found to be stable at pressures higher than 80 GPa. These discoveries suggest possible hydrogen storage in the mantle transition zone and in the mantle below 1800 km depths, respectively. However, it remains uncertain how the potential deep hydrogen storage can be connected to the shallower storage. Here, we report a new hydrous iron oxide ( $\eta$ -Fe<sub>12</sub>O<sub>18+x/2</sub>H<sub>x</sub>,  $x \approx 2$ ) stable at pressures between the stability fields of the  $\varepsilon$ - and the pyrite-type FeOOH. Our experiment also shows that the new  $\eta$  phase can exist together with the major lower mantle minerals including bridgmanite and periclase, making it an important hydrogen-bearing phase in the Earth's deep interior. Because of its limited H<sub>2</sub>O storage capacity, which is less than 1/6 of the storage capacity of the pyrite-type phase and the  $\varepsilon$  phase, the stability of the  $\eta$  phase would result in H<sub>2</sub>O loss during water transport in the mid mantle and therefore limit the amount of H<sub>2</sub>O potentially stored in the Fe–O–H system of the lower mantle. The large channel in the crystal structure of the  $\eta$  phase could provide potential storage sites for other volatile elements in the deep mantle.

© 2020 Elsevier B.V. All rights reserved.

## 1. Introduction

Hydrogen (H) is the most abundant element in the solar system. However, the amount of H stored in the Earth's interior, which is volumetrically dominant, remains uncertain. Hydrogen can be accommodated in nominally anhydrous minerals. To a depth of 410-km, major mineral phases in the upper mantle may contain a small amount of H, in the form of OH, at 100–500 ppm H<sub>2</sub>O (Michael, 1988). Laboratory experiments and diamond inclusion studies have shown that the mantle transition zone between depths of 410 and 660 km may contain much more H as OH in the main mineral phases (wadsleyite and ringwoodite) (Kohlstedt et al., 1996; Pearson et al., 2014) at least locally. The lower mantle represents

55% of the Earth's volume and therefore the possible storage of H in this region is important to the budget of H in the interior. However, the dominant minerals in the lower mantle, bridgmanite and ferropericlase, seem to have very low H<sub>2</sub>O storage capacities (Bolfan-Casanova et al., 2002; Panero et al., 2015).

Hydrous phases would form when nominally anhydrous phases are saturated with hydrogen (Hirschmann, 2006). Although the amounts of possible hydrous phases in the mantle are uncertain, the high concentrations of H in these phases provide possible storage for a significant amount of H in the deep mantle. Two recent experimental studies documented that  $\varepsilon$ -FeOOH (hereafter  $\varepsilon$ ), containing some Ti, is stable from 12–19 GPa at 1300 K in a hydrous mid-oceanic ridge basaltic (MORB) composition (Liu et al., 2018; Nishihara and Matsukage, 2016; Ono, 1998). Therefore,  $\varepsilon$ -FeOOH can be important for storage and transport of hydrogen in the upper mantle and the mantle transition zone. At pressures above 80 GPa, the pyrite-type FeOOH phase (hereafter py) is stable. However, the H content in the py phase is still under debate (Liu et al.,

\* Corresponding author at: School of Earth Sciences, China University of Geosciences, Wuhan, Hubei, China.

\*\* Corresponding author.

E-mail addresses: hchen156@asu.edu (H. Chen), SHDShim@asu.edu (S.-H. Shim).

**Table 1**  
Experimental runs conducted in this study. We include unit-cell parameters of the observed phases at high pressures and 300 K after laser heating. Temperature uncertainty is approximately 100 K. Other estimated  $1\sigma$  uncertainties are provided in parentheses. *P*: pressure, *T*: temperature, S.M.: starting materials, Med.: pressure transmitting medium, Ol: olivine, Hem: hematite, Goe: goethite,  $\eta$ : Fe<sub>12</sub>O<sub>19</sub>H<sub>2</sub>, py: pyrite-type FeOOH, and  $\varepsilon$ : CaCl<sub>2</sub>-type FeOOH.

Runs	<i>P</i> (GPa)	<i>T</i> (K)	S.M.	Med.	$\eta$			py <i>V</i> (Å <sup>3</sup> )	$\varepsilon$ <i>V</i> (Å <sup>3</sup> )
					<i>V</i> (Å <sup>3</sup> )	<i>a</i> (Å)	<i>c</i> (Å)		
103a	82(4)	1558	Hem	H <sub>2</sub> O	221.24(4)	10.01(1)	2.549(1)	88.33(2)	47.7(2)
103b	83(4)	1720	Hem	H <sub>2</sub> O	218.12(7)	9.93(3)	2.554(3)	87.79(7)	47.7(1)
204a	51(3)	1420	Hem	H <sub>2</sub> O					49.5(1)
204b	85(4)	1880	Hem	H <sub>2</sub> O				88.09(6)	47.6(1)
204c	93(5)	2008	Hem	H <sub>2</sub> O				87.08(4)	47.2(1)
204d	96(5)	1845	Hem	H <sub>2</sub> O				86.94(7)	
301a	96(5)	1675	Hem	H <sub>2</sub> O				86.89(7)	47.3(2)
301b	106(5)	2051	Hem	H <sub>2</sub> O				86.12(5)	
416	59(4)	1490	Hem	H <sub>2</sub> O					49.5(2)
417a	56(3)	1576	Hem	H <sub>2</sub> O	233.51(10)	10.23(5)	2.576(1)		49.6(1)
417b	63(3)	1556	Hem	H <sub>2</sub> O	230.82(10)	10.18(4)	2.572(2)		49.2(1)
417c	63(3)	2035	Hem	H <sub>2</sub> O	230.82(10)	10.18(4)	2.572(2)		49.2(1)
504	74(4)	1631	Hem	H <sub>2</sub> O	224.15(20)	10.07(5)	2.552(2)		47.9(1)
104a	64(3)	1400	Goe	Ne	234.21(15)	10.16(5)	2.624(2)		48.9(1)
104b	61(3)	1943	Goe	Ne	234.21(15)	10.16(5)	2.624(2)		48.9(1)
612	67(3)	1500	Goe	H <sub>2</sub> O	233.29(15)	10.14(5)	2.620(2)		
ol18a	99(3)	2160	Ol	H <sub>2</sub> O	230.8(15)			85.64(10)	
ol18b	106(3)	2176	Ol	H <sub>2</sub> O				85.39(10)	

2017; Nishi et al., 2017). A series of hydrous phases have been discovered at the lower mantle conditions, most notably CaCl<sub>2</sub>-type structured phases, such as  $\delta$ -AlOOH,  $\varepsilon$ -FeOOH, and H-MgSiO<sub>2</sub>(OH)<sub>2</sub> (phase H), and pyrite-type structured phases, such as py-FeO<sub>2</sub>H<sub>x</sub> ( $x < 1$ ) and py-FeOOH (Liu et al., 2017; Nishi et al., 2017, 2014; Sano et al., 2008; Suzuki et al., 2000). These phases appear to form solid solutions with each other in the mantle-related chemical systems (Nishi et al., 2019, 2015; Ohira et al., 2014; Pamato et al., 2015; Yuan et al., 2019). Therefore, it is important to know if the water storage in the shallow mantle can be connected to the potential storage in the deep mantle.

For Fe–O–H system, far fewer data points – and larger gaps between them – exist at the mid-mantle *P*–*T* conditions. Therefore, it is unclear if the  $\varepsilon$  phase (a low-pressure polymorph) transitions directly to the py phase or if an intermediate phase exists between the  $\varepsilon$  and py phases. This uncertainty raises a question of whether hydrous iron oxide can play a role in the hydrogen (or “water”) cycle for a large depth range of the mantle. Here, we report a series of experiments on Fe–O–H systems conducted at the *P*–*T* conditions of the mid-mantle in the laser-heated diamond-anvil cell (Table 1). We discovered a new hexagonal phase (hereafter  $\eta$ ) in the system at 56–83 GPa and high temperatures. Even though it can be formed in a water-saturated system, the  $\eta$  phase contains a much smaller amount of H<sub>2</sub>O compared with the  $\varepsilon$  and py phases.

## 2. Methods

### 2.1. Laser heated diamond anvil cell

We loaded pure hematite or goethite (Alfa-Aesar) pre-pressed foil to a symmetric diamond anvil cell (DAC) chamber. Either H<sub>2</sub>O or Ne was loaded as a pressure medium. Olivine (Mg<sub>0.94</sub>Fe<sub>0.06</sub>)<sub>2</sub>SiO<sub>4</sub> was loaded with H<sub>2</sub>O in a separate experiment to examine the stability of hydrous iron oxides in Mg-rich mantle related systems. Detailed information on experimental runs can be found in Table 1. Diamond anvils with 200  $\mu$ m culets and 150  $\mu$ m beveled culets were used for experiments at pressures lower and higher than 65 GPa, respectively. An indented rhenium gasket was drilled for a sample chamber with a 90 or 120  $\mu$ m in diameter, depending on the culet size. We loaded a gold particle in the sample chamber for pressure calculation from the measured unit-cell volume (Ye et al., 2017). To prevent potential alloying between Fe and Au at high pressures, the Au grain was separated from the sample

foils. We placed a few spacer grains less than 10  $\mu$ m below and above the sample foil to form layers of pressure medium between the sample and diamond anvils for thermal insulation. The spacer grains were chosen from the starting materials.

### 2.2. X-ray diffraction

We measured X-ray diffraction (XRD) patterns of the sample in the laser-heated DAC at beamline 13IDD and 13BMC at the GeoSoilEnviroCARS (GSECARS) sector (Prakapenka et al., 2008; Zhang et al., 2017) of the Advanced Photon Source. Monochromatic X-ray beams with beam sizes of 3  $\times$  4  $\mu$ m<sup>2</sup> and 12  $\times$  18  $\mu$ m<sup>2</sup> at 13IDD and 13BMC, respectively, were focused on the sample. We have collected diffraction data for samples with an X-ray wavelength of 0.4133 or 0.434 Å with a Pilatus detector. For heating, two near-infrared laser beams (1  $\mu$ m wavelength) were focused on the sample through both sides of DAC with a hot spot size of 20–25  $\mu$ m<sup>2</sup> at beamline 13IDD. The laser beams were aligned coaxially with the X-ray beam so that we can measure diffraction patterns from the center of the heating spots. Temperatures of the sample were calculated by fitting the thermal radiation spectra to the Planck equation from both sides of the sample. In each run, we heated the samples for at least 10 min. In run 612, to obtain a single phase, we heated the sample for 2 hr. We conducted diffraction pattern measurements both during laser heating and at 300 K before and after laser heating. At high temperatures, we calculated thermal pressures from the thermal expansion factor of ice VII (Fei et al., 1993). Except for heating run 104 which was conducted at Arizona State University, all the heating was conducted at APS. The measured diffraction images (Fig. 1 and S1) were integrated to diffraction patterns in the Dioptas package (Prescher and Prakapenka, 2015). We performed phase identification and peak fitting using a pseudo-Voigt profile shape function in the PeakPo package (Shim, 2017). The crystal structure was obtained from powder patterns in Endeavour, Fox, and Superflip (Favre-Nicolin and Černý, 2002; Palatinus and Chapuis, 2007; Putz et al., 1999). Rietveld refinements were performed with the general structure analysis system (GSAS-II) (Toby and Von Dreele, 2013). We refined phase fractions first, then atomic positions, lattice parameters and spherical harmonic terms for preferred orientation. After reaching a good visual fit, we refined all the parameters together to further reduce residuals after background subtraction,  $R_{wp-bknd}$ . We achieved  $R_{wp-bknd} < 1.8\%$  in all the refinements.

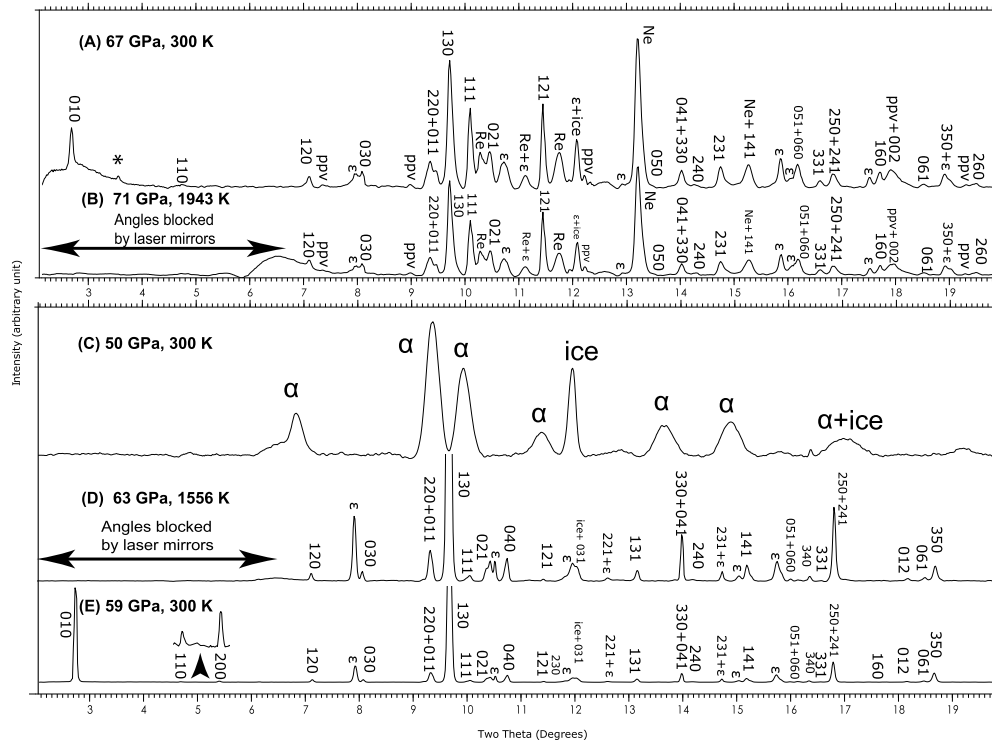


**Fig. 1.** X-ray diffraction patterns of the new  $\eta$  phase at high  $P$ - $T$ . The top panel shows diffraction patterns from an experiment with a goethite starting material in a Ne medium (A) after laser heating and (B) during laser heating at 71 GPa and 1943 K. The bottom panel shows the  $\eta$  phase formed from laser heating of an  $\text{Fe}_2\text{O}_3$  hematite starting material in an  $\text{H}_2\text{O}$  medium (C) before laser heating, (D) during laser heating at 63 GPa and 1556 K, and (E) after laser heating. The inset in (E) shows zoom-in view for 110 and 200 peaks. We show the Miller indices for the  $\eta$  phase. The wavelength of the X-ray beam was 0.4133 Å. Phase identification:  $\alpha$ : hematite,  $\varepsilon$ :  $\varepsilon$ -FeOOH, ppv:  $\text{Fe}_2\text{O}_3$  ice: ice VII, Ne: Neon pressure medium, and \*: unidentified line.

### 2.3. Synchrotron Mössbauer Spectra of the $\eta$ phase

For the Mössbauer data, the sample was synthesized from a  $\text{Fe}_2\text{O}_3 + \text{H}_2\text{O}$  mixture at 62 GPa and 1600 K in LHDAC. In order to enhance the Mössbauer signal, we used  $^{57}\text{Fe}$  enriched (67%)  $\text{Fe}_2\text{O}_3$ . X-ray diffraction of the sample indicates that the majority of the sample is the  $\eta$  phase with a small amount of the  $\varepsilon$  phase. Nuclear forward scattering was conducted at sector 3 of APS. We focused a 14.4-keV X-ray beam on an area of  $6 \times 6 \mu\text{m}^2$  in the sample. The storage ring was operated in top-up mode with 24 bunches separated by 153 ns. We measured nuclear resonant scattering in a time window of 15–130 ns with a data collection time of 30 min. We measured synchrotron Mössbauer spectra at high pressure after temperature quench (Fig. S2).

The fitting was performed for the measured spectrum using the CONUSS package (Sturhahn, 2000). At the beginning of all the spectral fittings, we conducted Monte-Carlo search in CONUSS in order to avoid non-uniqueness of the optimized fitting solutions. Because we detected a small amount of the  $\varepsilon$  phase from XRD for the sample we used for Mössbauer spectroscopy, we included the Mössbauer parameters of the  $\varepsilon$  phase obtained from a separate measurement for pure  $\varepsilon$  phase (to be reported elsewhere). For the isomer shift, we measured a separate spectrum with the sample and a  $\text{FeSO}_4 \cdot 7\text{H}_2\text{O}$  standard.

### 2.4. First-principles calculations of the $\eta$ phase

First-principles calculations were performed within the framework of density functional theory (DFT) (Hohenberg and Kohn, 1964; Kohn and Sham, 1965), as implemented in Vienna Ab initio Simulation Package (VASP) code (Kresse and Furthmüller, 1996). Projector augmented wave (PAW) potentials were used in all the calculations to describe the interactions between core and valence

electrons (Blöchl, 1994). Considering the good agreement between the experimental and the simulated lattice parameters in a Fe–O–H system in a previous study (Lu and Chen, 2018), we implemented Perdew–Burke–Ernzerhof (PBE) functional (Perdew et al., 1996) for the exchange–correlation interactions of electrons. Plane-wave basis with a cutoff energy of 500 eV and  $k$ -point sampling of  $2\pi \times 0.025 \text{ \AA}^{-1}$  were employed to obtain the precise total energy at 0 K (without zero-point vibration) and 40 to 85 GPa (approximately to experimental pressures). We relaxed the crystal structure until all the stress forces of atoms were smaller than 0.01 eV/Å.

## 3. Results

### 3.1. A new iron oxide phase in Fe–O–H at high pressure-temperature

In our laser-heated diamond-anvil cell (LHDAC) experiments with a hematite starting material in an  $\text{H}_2\text{O}$  medium at 63 GPa and 1556 K, at least nine new diffraction lines were observed whereas the diffraction peaks from hematite disappeared (Fig. 1). Similar diffraction pattern was observed with  $\alpha$ -FeOOH in a Ne medium at 64 GPa and 1700 K (Table 1). The new peaks appeared within two minutes of laser heating and grew steadily with heating. After temperature quench, for better coverage toward the lower  $2\theta$  angles (i.e., higher  $d$ -spacings), the laser mirrors were removed from the X-ray beam path, enabling the detection of high  $d$ -spacing lines up to 9.6 Å. We found a diffraction line at  $d$ -spacing 8.856 Å. This low angle line was the key when constraining the shape of the unit cell (Fig. 1c). The new lines were not associated with any known polymorphs of  $\text{Fe}_2\text{O}_3$  (including hematite, post-perovskite,  $\text{Rh}_2\text{O}_3$ -II type phases, and other iron oxide stable at the pressure range) (Bykova et al., 2016),  $\text{FeH}_x$  (dhcp and fcc), FeOOH ( $\varepsilon$  and py phases), or  $\text{H}_2\text{O}$ . At the beginning of laser heating, weak  $\varepsilon$  peaks were observed at 56–83 GPa and 1400–1720 K. With further heating, the peaks of the  $\varepsilon$  phase become weaker while the intensity

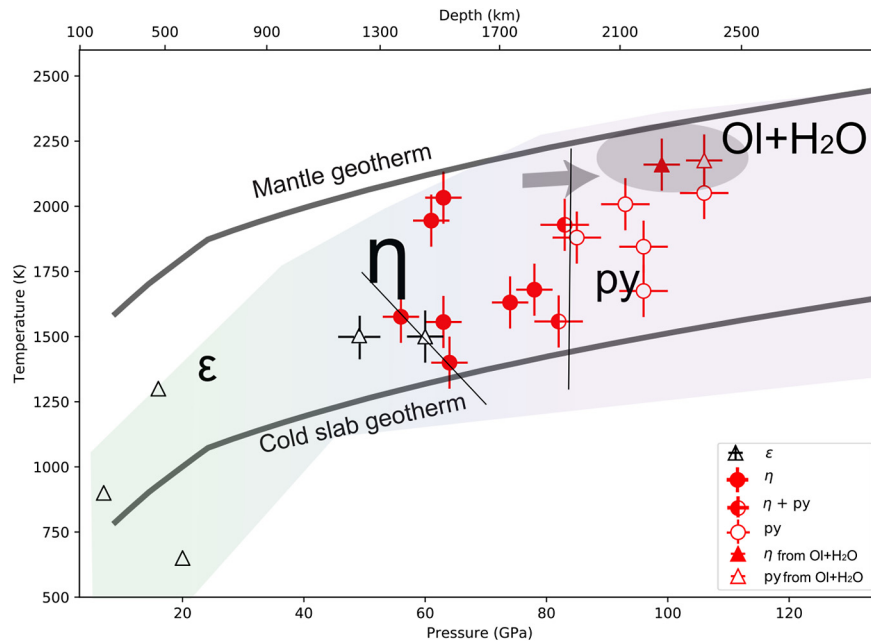


**Fig. 2.** The pressure-temperature conditions for the phases observed in Fe–O–H and Fe–Mg–Si–O–H systems. The closed and open circles indicate the observations of the  $\eta$  and py phases in our experiments, respectively. The half-filled circles are for observations of the  $\eta + \text{py}$  phases in our experiments. The data points from previous studies are shown for the  $\epsilon$  phase in open triangles (Dyuzheva et al., 2006; Gleason et al., 2008; Nishi et al., 2017; Nishihara and Matsukage, 2016). The mantle geotherm is from Brown and Shankland (1981). The two thin lines show the conditions where phase changes were observed. The thick gray arrow indicates potential expansion of the  $P$ – $T$  stability of the  $\eta$  phase in Mg–Fe–Si–O–H system.

of the  $\eta$  phase increases at these  $P$ – $T$  conditions. Therefore, the  $\eta$  phase is likely the high temperature phase of the  $\epsilon$  phase at 56–83 GPa.

The py phase appeared together with the  $\eta$  phases at 83 GPa and 1720 K (also a small amount of the  $\epsilon$  phase). Above this pressure, the  $\eta$  phase disappeared and the py phase became dominant, with a small amount of the  $\epsilon$  phase in diffraction patterns (Runs 103 and 301 in Table 1; Fig. S3). Therefore, the stability field of the  $\eta$  phase is located at a lower pressure than that of the py phase, while likely at a higher pressure than the  $\epsilon$  phase (Fig. 2). The Fe–O–H system has been investigated at high  $P$ – $T$  in recent years (Gleason et al., 2013; Hu et al., 2016; Liu et al., 2017; Nishi et al., 2017). These studies, however, explored mostly pressures where the  $\eta$  phase is unstable. A study reported py-FeO<sub>2</sub>H<sub>x</sub> at 72 GPa and 2300 K (Hu et al., 2017), close to where we begin to observe a transition from the  $\eta$  phase to the py phase (Fig. 2). However, diffraction patterns were not reported for those  $P$ – $T$  conditions. Another study examined FeOOH, reporting it as the possible  $\epsilon$  phase at 59 GPa and 2000 K and 79 GPa and 2100 K (Hu et al., 2016), but X-ray diffraction pattern for the observation was not reported.

### 3.2. Crystal structure of the $\eta$ phase

Although first principles and experimental studies have discovered some iron oxide phases at high pressures (Bykova et al., 2016; Weerasinghe et al., 2015), none of the existing structures fit our diffraction patterns. In order to solve the crystal structure of the  $\eta$  phase, we conducted a series of analyses presented in the supplementary information using both powder diffraction patterns and textured diffraction images.

Briefly, we first explored candidate space groups from the systematic absence of certain diffraction lines, resulting in  $P6_3$  and  $P6_3/m$ . We then conducted simulated annealing and ab initio assisted Monte Carlo method to solve the crystal structure from powder diffraction patterns in the Endeavour and the Fox packages (Favre-Nicolin and Černý, 2002; Putz et al., 1999). The crystal struc-

ture model we obtained in this way was then used as a starting structure model for Rietveld refinements in GSAS-II (Toby and Von Dreele, 2013). The new crystal structure model yielded a 12:19 molar ratio between Fe and O. The crystal structure solution was also confirmed through comparison with the textured diffraction images (Fig. S1 and Table S1).

The structural model for the  $\eta$  phase has two crystallographic sites for Fe (Fig. 3 and Table S2). One half of Fe is 6-fold coordinated while the other half is 7-fold coordinated (Fig. 3c). The 7 coordinated Fe has a capped trigonal prism arrangement of six O atoms with an additional O atom (i.e., 6 + 1 coordinated Fe). Similar coordination of Fe was also found in an Fe-oxide polymorph at 80 GPa (Bykova et al., 2016). The crystal structure had the corner sharing FeO<sub>6</sub> octahedra and the six FeO<sub>6</sub> octahedra formed a hexagonal channel at the [001] edges of the unit cell, similar to the structure documented in a high-pressure polymorph of CaMg<sub>2</sub>Al<sub>6</sub>O<sub>12</sub> called the new aluminum phase (NAL) phase (Miura et al., 2000). The FeO<sub>7</sub> polyhedra were connected with the FeO<sub>6</sub> octahedra by sharing the edges while two layers of FeO<sub>7</sub> have face sharing. This type of face sharing is also shown for the Mg sites with a trigonal prism arrangement in the NAL phase (Miura et al., 2000).

### 3.3. Synchrotron Mössbauer Spectra (SMS) of the $\eta$ phase

Our Mössbauer measurements for the  $\eta$  phase identified three different Fe sites (Fig. S2 and Table S3). Two of the three sites have Mössbauer parameters consistent with low-spin Fe<sup>3+</sup> with a 1:0.8 ratio between them in fraction. The third site appears to be a high-spin Fe<sup>3+</sup> site, but its fraction is close to the estimated uncertainty while the other two  $\eta$  sites are more than 10 times greater in fractions and therefore more dominant. The fractions of these two dominant sites and their Mössbauer parameters are consistent with our crystal structure model of the  $\eta$  phase from experimental data in that: (1) there exist largely two Fe sites and the ratio between them is close to 1:1. As we discuss below, we also found

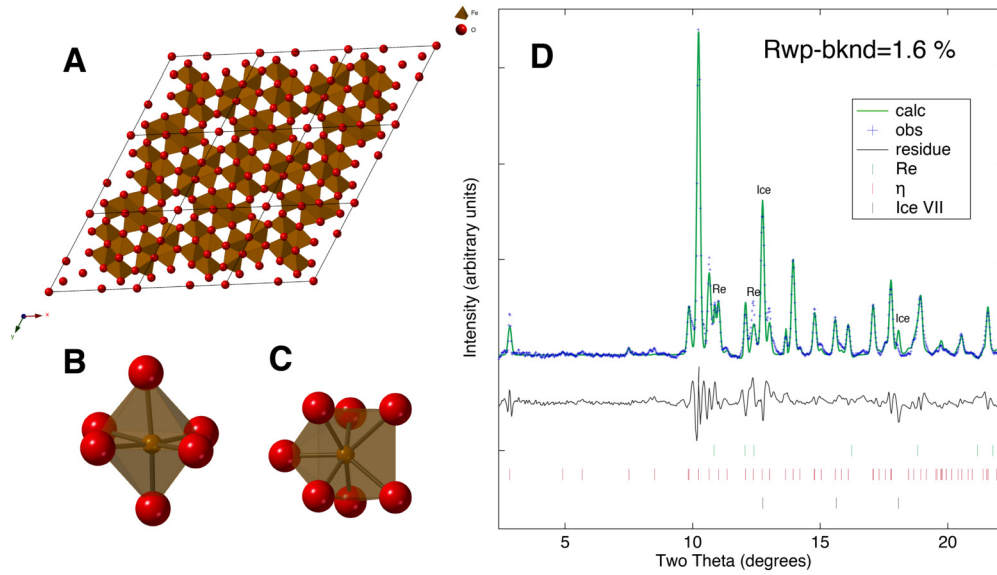
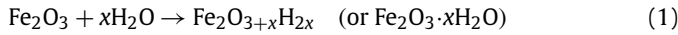


**Fig. 3.** The crystal structure model for the  $\eta$  phase from Rietveld refinements. (A) The crystal structure of the  $\eta$  phase along the  $c$  axis. (B and C) The Fe–O polyhedral with 6 and 7-fold coordination, respectively. (D) The Rietveld refinement for a diffraction pattern measured at 62 GPa and 300 K after laser heating:  $a = 10.14(1)$  Å and  $c = 2.62(1)$  Å for the  $\eta$  phase, and  $a = 2.70(1)$  Å for ice VII. The wavelength of the X-ray beam was 0.434 Å.

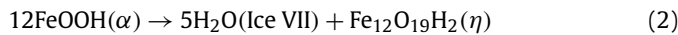
that our Mössbauer result is consistent with our first-principles calculations: Fe are likely low-spin  $\text{Fe}^{3+}$ .

#### 3.4. Estimation for the hydrogen content in the $\eta$ phase

For experiments with starting materials of  $\text{Fe}_2\text{O}_3$  and  $\text{H}_2\text{O}$ , products of the possible chemical reaction between them should exist on a tie line between these two compositions. The final product should be then:



For example, when  $x = 1$ , the reaction will produce  $\text{FeOOH}$ . In contrast, for the laser heating of a goethite starting material in a Ne medium,  $\text{H}_2\text{O}$  exists only in the starting  $\alpha\text{-FeOOH}$ ; therefore, the amount of  $\text{H}_2\text{O}$  is limited. In this experiment, we observed the formation of ice VII as well as the  $\eta$  phase (Fig. 1d). The reaction in this experiment can be written as:



Although anhydrous  $\text{ppv-Fe}_2\text{O}_3$  peaks were also observed in some of the diffraction patterns, they were much smaller in intensity compared with other phases and therefore we ignored  $\text{ppv-Fe}_2\text{O}_3$  in the reaction above. Our measured unit-cell volumes of the  $\epsilon$  and pyrite-type phases are consistent with the reported values (Gleason et al., 2013; Nishi et al., 2017) at high pressure and 300 K (Fig. 4). For the py phase, our unit-cell volume values are close to the fully hydrated version of the phase,  $\text{py-FeOOH}$ . The unit-cell volume of the  $\eta$  phase is smaller than those of both  $\epsilon$  and py phases, meaning that less  $\text{H}_2\text{O}$  exists in the  $\eta$  phase than the py phase.

$\text{Py-FeOOH}$  is not quenchable at 1 bar (Hu et al., 2017) and therefore is impossible to measure its unit-cell volume and hydrogen content at 1 bar (Chen et al., 2019; Hu et al., 2017). Hu et al. (2017) used the unit-cell volume difference between the dry and hydrated forms of  $\text{FeO}_2$  and attributed the difference to the effect of H. We conducted similar calculations here. For the  $\epsilon$  and  $\eta$  phases, no dry form is known, unlike the py phase. Because the  $\epsilon$  and  $\eta$  phases can be written in a form of  $\text{Fe}_2\text{O}_3 \cdot x\text{H}_2\text{O}$ , we adapted post-perovskite type (ppv)  $\text{Fe}_2\text{O}_3$ , which is stable form for  $\text{Fe}_2\text{O}_3$  at this pressures (56–83 GPa), as a dry form (Shim et al., 2009).

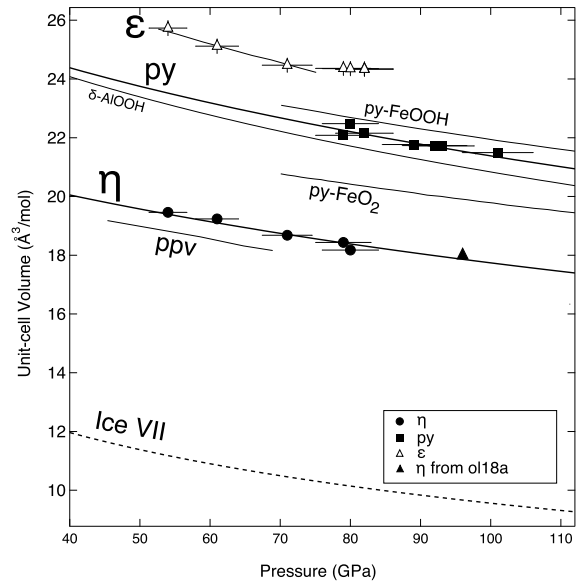


**Fig. 4.** The unit-cell volume of the  $\eta$  phase at high pressure and 300 K. The unit-cell volumes are normalized by the number of Fe or Al atoms in the unit cells. We also show the unit-cell volumes of the  $\epsilon$  and py phases measured in this study. We include the compressional curves of  $\text{py-FeO}_2$  (Hu et al., 2017), py (Hu et al., 2017),  $\epsilon$  (Gleason et al., 2013),  $\text{ppv-Fe}_2\text{O}_3$  (Bykova et al., 2013),  $\delta\text{-AlOOH}$  (Mashino et al., 2016) and ice VII (Wolaniin et al., 1997) for comparison. The thick lines are calculated values from the equation of state for the py and  $\eta$  phases (see section 3.5 for detail).

The reason we choose  $\text{ppv-Fe}_2\text{O}_3$  as a dry form to compare is that  $\text{ppv-Fe}_2\text{O}_3$  has a similar atomic arrangement for the Fe–O bonds. Both  $\text{ppv-Fe}_2\text{O}_3$  and  $\eta$  phase have two iron positions: one with the  $\text{FeO}_6$  octahedral coordination and the other with the  $\text{FeO}_6$  trigonal prism coordination (Murakami et al., 2005; Shim et al., 2009). The ratio is 1:1 in both crystal structures. Thus, from crystallographic consideration, the two structures could have a similar unit-cell volume. If anhydrous, however, the  $\eta$  phase should have a smaller unit-cell volume than  $\text{ppv-Fe}_2\text{O}_3$ , because the  $\eta$  phase is stable at higher pressures. However, we observed slightly larger unit-cell volume for the  $\eta$  phase. Thus, the most reasonable explanation is the existence of water in the crystal structure of the

$\eta$  phase but very small amount. The approach has limitations in that the dry forms in  $\text{Fe}_2\text{O}_3$  and hydrous forms have different crystal structures. Nevertheless, the calculation presented below provides some qualitative insights into the content of  $\text{H}_2\text{O}$  in the  $\eta$  phase.

At 60 GPa, the unit-cell volume of  $\varepsilon$  is  $25.12 \text{ \AA}^3$  for  $V/x(\text{Fe})$  (Fig. 4), which is a unit-cell volume divided by the number of Fe atoms in the unit cell,  $x(\text{Fe})$ . The value is consistent with the results from Gleason et al. (2013). At the pressure, the post-perovskite type structure (ppv) becomes stable in  $\text{Fe}_2\text{O}_3$ , which we take as a dry form. The ppv- $\text{Fe}_2\text{O}_3$  has  $V/x(\text{Fe}) = 18.55 \text{ \AA}^3$  at 60 GPa. The volume difference between the  $\varepsilon$  and the ppv- $\text{Fe}_2\text{O}_3$  can be approximately attributed to the volume occupied by  $\text{H}_2\text{O}$  in the crystal structure of the  $\varepsilon$  phase. Therefore, we can obtain  $\Delta V/x(\text{Fe}) = 6.57 \text{ \AA}^3$  for  $0.5\text{H}_2\text{O}$ .

The  $\eta$  phase has a larger unit-cell volume than ppv- $\text{Fe}_2\text{O}_3$  by  $\Delta V/x(\text{Fe}) = 0.62 \text{ \AA}^3$  at 60 GPa. Then, we calculated the unit-cell volume for the  $\eta$  phase with one Fe atom to be  $19.17 \text{ \AA}^3$  at 60 GPa. If the rate of the unit-cell volume change we measured above between the  $\varepsilon$  phase and ppv- $\text{Fe}_2\text{O}_3$  was applicable between the  $\eta$  and ppv phases, we obtain  $0.05\text{H}_2\text{O}$  for 1 mol of  $\text{FeO}_{1.5}$ . We chose  $\varepsilon\text{-FeOOH}$  as the fully hydrous form to compare the unit-cell volumes because its hydration state and equation of state are better known than those of the py phase.

For the  $\eta$  phase, we estimated  $\text{Fe}_{12}\text{O}_{18.6}\text{H}_{1.2}$  ( $0.05\text{H}_2\text{O}$  per  $\text{FeO}_{1.5}$ ) for an ideal composition. The water site in the crystal structure is "Ow" in Table S2. The exact amount of H in the  $\eta$  phase remains uncertain because of the limitations in the methods we used above. The  $\eta$  phase is not quenchable in our experiment, preventing us from conducting further analysis on the amount of  $\text{H}_2\text{O}$ . However, our analysis above strongly suggests that the  $\text{H}_2\text{O}$  content in the  $\eta$  phase should be lower than those in the  $\varepsilon$  and py phases. The low  $\text{H}_2\text{O}$  content in the  $\eta$  phase can be further supported by our experiments with a goethite ( $\alpha\text{-FeOOH}$ ) starting material in a Ne medium at 64 GPa and 1900 K (Eq. (2) and Fig. 1d) where we detected formation of  $\text{H}_2\text{O}$  ice by heating.

### 3.5. The bulk modulus of the $\eta$ phase

The  $\eta$  phase is not quenchable to 1 bar and therefore we could not obtain unit-cell volume at 1 bar,  $V_0$ . Therefore, we fit for  $V_0$  and bulk modulus at 1 bar,  $K_0$ , by fixing the pressure derivative of  $K_0$ ,  $K'_0$  to 4. Fitting was conducted for our dataset measured at 56–83 GPa to the Birch-Murnaghan equation of state. We obtained a bulk modulus of 202(15) GPa with a volume projected to 1 bar of  $282(2) \text{ \AA}^3$ . This bulk modulus value is intermediate between those for the  $\varepsilon$  phase ( $K_0 = 132$  and  $162$  GPa for high spin and low spin, respectively; Gleason et al., 2013) and pyrite-type phase ( $K_0 = 220(30)$  GPa with  $V_0 = 112(4) \text{ \AA}^3$  from this study by fitting data from 79–101 GPa for  $K'_0 = 4$ ).

### 3.6. First-principles calculations for the $\eta$ phase

We performed density-functional theory (DFT) calculations for the Fe–O–H system at 40–80 GPa to examine the crystal structure and the enthalpy of the  $\eta$  phase. The crystal structure from the DFT calculations agreed well with the crystal structure model from our experiments even without  $\text{H}_2\text{O}$ :  $P6_3/m$  space group with a starting composition  $\text{Fe}_{12}\text{O}_{18}$ . However, without  $\text{H}_2\text{O}$  in the crystal structure, the enthalpy of  $\eta\text{-Fe}_{12}\text{O}_{18}$  was higher than ppv- $\text{Fe}_2\text{O}_3$  (Fig. S4), implying that the new  $\eta\text{-Fe}_{12}\text{O}_{18}$  phase is thermodynamically less stable than ppv- $\text{Fe}_2\text{O}_3$ . From our experimental results, 0.5–1 mole of  $\text{H}_2\text{O}$  may exist in the  $\eta$  phase. Thus, we relaxed the crystal structure with 0.5 and 1 mole  $\text{H}_2\text{O}$  in the channel.

After structural optimization, the  $P6_3/m$  was retained in the  $\text{Fe}_{12}\text{O}_{18.5}\text{H}$  if we ignored the H atom positions. However, when

we relaxed the  $\text{Fe}_{12}\text{O}_{19}\text{H}_2$ , it transformed to a triclinic cell with  $\alpha = 89^\circ$ ,  $\beta = 91^\circ$ , and  $\gamma = 119.1^\circ$ . The magnitudes of the  $a$  and  $c$  parameters of the triclinic cell were in agreement with the hexagonal parent cell as shown in Fig. S4. Overall, the unit-cell volume and the unit-cell parameters observed in our experiments lie in between those of  $\text{Fe}_{12}\text{O}_{18.5}\text{H}$  and  $\text{Fe}_{12}\text{O}_{19}\text{H}_2$  from the DFT calculations. The similarity in the unit-cell parameters supports our inference on 0.5–1 mole of  $\text{H}_2\text{O}$  in the  $\eta$  phase from our experimental data. The two crystallographic sites of Fe were also confirmed: two sites with six and seven coordination numbers in the low-spin state which is consistent with our Mössbauer data. The O–H bonding at 80 GPa is  $0.97 \text{ \AA}$ , where hydrogen atom lies in between the O–O atoms but asymmetrically in the channel at the four side edges of the unit cell (Fig. 3). The hydrogen atom is located at (0, 0, 0.59) and (0, 0, 0.36) with half occupancy at 80 GPa from the calculations of  $\text{Fe}_{12}\text{O}_{18.5}\text{H}$ .  $\text{Fe}_{12}\text{O}_{19}\text{H}_2$  has a hydrogen position of (0.96, 0.97, 0.18), which is off-centered at 80 GPa. The Fe–O bond distance in  $\text{FeO}_6$  is  $1.73\text{--}1.84 \text{ \AA}$  from the calculations, which are comparable to the values we obtained from experiments ( $1.78\text{--}1.88 \text{ \AA}$ ) at 80 GPa. The anisotropic Fe–O bond distances are required to form a channel that is also observed in the NAL phase (Miura et al., 2000). The trigonal prism  $\text{FeO}_6$  had the Fe–O bonding of  $1.93\text{--}1.96 \text{ \AA}$  from the calculation, while Rietveld refinements yielded  $1.90\text{--}1.97 \text{ \AA}$ . The trigonal prism  $\text{FeO}_6$  contains another Fe–O bonding with a distance of  $2.03$  and  $2.05 \text{ \AA}$  in calculations and experimental results, respectively, at 80 GPa. Overall, the Fe–O bond properties from Rietveld refinements agree with the DFT calculations.

The calculated enthalpy of the  $\text{Fe}_{12}\text{O}_{19}\text{H}_2$  phase is lower than ppv- $\text{Fe}_2\text{O}_3 + \text{Ice VII}$ , while  $\text{Fe}_{12}\text{O}_{18.5}\text{H}$  has a slightly higher energy (e.g.,  $48 \text{ meV/atom}$ ) than ppv- $\text{Fe}_2\text{O}_3 + 0.5 \text{ Ice VII}$  (Fig. S4 d and e). However, considering high-temperature conditions in our experiments, the thermal energy (e.g.  $138 \text{ meV/atom}$  at 1600 K) is comparable to the energy difference evaluated at 0 K by DFT. At least, the close energy between the  $\eta$  phase and ppv- $\text{Fe}_2\text{O}_3 + \text{ice VII}$  supports the existence of  $\text{H}_2\text{O}$  in the crystal structure of the  $\eta$  phase and its estimated  $\text{H}_2\text{O}$  content between  $\text{Fe}_{12}\text{O}_{18.5}\text{H}$  and  $\text{Fe}_{12}\text{O}_{19}\text{H}_2$ .

The exact description of strongly correlated electron systems, such as ppv- $\text{Fe}_2\text{O}_3$  and the  $\eta$  phase present here, is still challenging in DFT (Meng et al., 2016). Also, the precise total energy calculations through DFT can be limited by the structural uncertainty derived from the varying ratios of  $\text{H}_2\text{O}$  and positions of extra O and H atoms in the  $\eta$  phase. However, our theoretical results generally align with our experimental results (in both lattice parameters and energy differences) and support much lower  $\text{H}_2\text{O}$  content of the  $\eta$  phase than the  $\varepsilon$  and py phases.

### 3.7. Stability of the $\eta$ phase in the lower mantle chemical system

In our experiments with an olivine + water starting mixture at 99 GPa and 1700 K, the  $\eta$  phase was formed together with bridgmanite, periclase, and the py phase (Fig. 5). At pressures above 99 GPa, we observed the coexistence of the py phase with bridgmanite and periclase. A recent experiment showed that the py phase can co-exist with bridgmanite and post-perovskite at the conditions of the Earth's deep mantle (Yuan et al., 2019), which is consistent with our result in O118b in Table 1. The experimental observation suggests that the  $\eta$  phase can appear in the Mg-rich mantle systems if  $\text{H}_2\text{O}$  is present in the system.

We also note that Yuan et al. (2019) observed a weak diffraction peak from py- $\text{FeOOH}$  in their diffraction patterns. Our py peaks are more intense than the one reported from Yuan et al. (2019) despite the fact that our starting material contains less Fe (6 mol%) than Yuan et al. (2019). We calculated X-ray diffraction pattern of 94 mol% Brd + 6 mol% py- $\text{FeOOH}$  (see Fig. S5) using the Crystal-

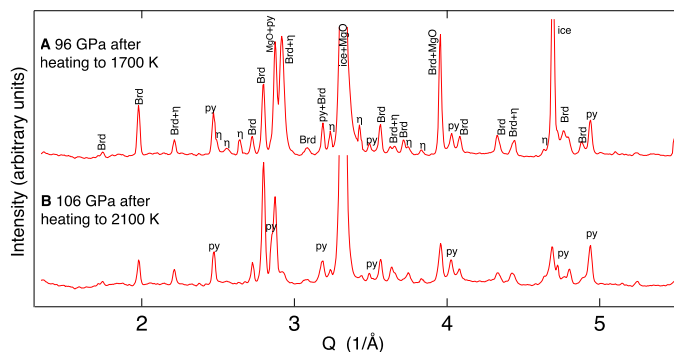


**Fig. 5.** X-ray diffraction patterns from olivine + H<sub>2</sub>O experiments: (A) Brd, Fp,  $\eta$  and py phases at 96 GPa and (B) Brd, Fp, and pyrite phase at 106 GPa in our experiments. In the plot,  $Q$  ( $Q = 2\pi/d$ , where  $d$  is  $d$ -spacing) is used for the x-axis.

Maker and CrystalDiffract software (Palmer, 2015). The calculation shows that the cubic py-FeOOH has significant intensity even if the concentration is only 6 mol%. The reasons are: (1) Fe had more electrons thus the scattering factor for the py phase is higher, and (2) the diffraction peaks of the cubic py-FeOOH have higher multiplicities than those of orthorhombic Brd.

There are several possible reasons why Yuan et al. (2019) have low intensity for the peaks of py-FeOOH. First, we used a much larger amount of water that would form more hydrous phases. In contrast, much less water was available in the system of Yuan et al. (2019), 6–7 wt%. Yuan et al. (2019) observed some Fe remaining in bridgmanite, suggesting that not all the Fe was used for forming FeOOH in their experiments. Secondly, the partitioning of Fe into  $\delta$ -AlOOH and Brd/ppv undoubtedly affects the amount of FeOOH in the system. Yuan et al. (2019) used 30 mol% Al in the sample which are significantly higher than the pyrolitic composition. We note that  $\varepsilon$ -FeOOH and  $\delta$ -AlOOH can form a solid solution (Nishi et al., 2019). Thus the formation of  $\delta$ -AlOOH in Yuan et al. (2019) and therefore possible existence of Fe in the phase would reduce the XRD intensity for py-FeOOH in their experiments. A recent study on a similar chemical system reported that Mg can substitute for Fe in py-FeOOH<sub>x</sub> (Hu et al., 2020). The substitution would increase the amount of the py phase, which can result in higher peak intensity of py-FeOOH found in our diffraction patterns compared with Yuan et al. (2019).

The pressure where we found the  $\eta$  phase in olivine + water starting material (99 GPa) is higher than the pressure where the phase was observed in Fe–O–H system (<83 GPa). It can be hypothesized that other elements in the olivine + water experiment may stabilize the  $\eta$  phase to higher pressures. This opens up an intriguing possibility that Mg or Si can dissolve into the  $\eta$  phase.

#### 4. Implication and conclusion

The new  $\eta$  phase is stable at the lower pressure side of the py phase stability field while it is stable at higher  $P$ – $T$  than the  $\varepsilon$  phase. The exact amount of H<sub>2</sub>O in the new hydrous iron oxide ( $\eta$  phases) remains tentative at 2 wt% at the pressure range 56–83 GPa. However, the unit-cell volume from our experiment and the DFT calculation provide strong indication that the amount of H<sub>2</sub>O is lower than those in the  $\varepsilon$  and py phases, despite its stability under H<sub>2</sub>O saturated conditions in our experiments. Because of its lower H<sub>2</sub>O storage capacity, the  $\eta$  phase will substantially reduce the amount of H<sub>2</sub>O transported deeper into the lowermost mantle in Fe–O–H system, where the py phase would be stable. The potential importance of this new phase for the lower mantle can be further supported by our observation of the coexistence of the  $\eta$  phases together with bridgmanite and ferropericlase in our olivine + H<sub>2</sub>O experiments.

The hydrogen content in the lower mantle is not well constrained. Some amount of hydrogen could be subducted to the deep interior by subducting slabs (Peacock, 1990). If so, the aluminum or iron-rich hydrous phases, for example  $\varepsilon$ -FeOOH, could play an important role for the transportation of water. The titanium bearing  $\varepsilon$ -FeOOH was discovered at 12–19 GPa and 1300 K (Liu et al., 2018; Ono, 1998). Thus, MORB can be the water resource for the deep interior even to the depth of the core–mantle boundary if the slabs could be subducted to that depth. However, our result indicates that substantial amount of water would be lost during the phase transition from  $\varepsilon$ -FeOOH to the  $\eta$  phase.

The composition of the lithospheric mantle is different from MORB (Griffin et al., 2009). Phase H might form under a hydrous condition after the dehydration of phase D (Nishi et al., 2014). However, phase H has a relative limited stability field ranging from 35 to 60 GPa (Ohtani et al., 2014). Aluminum-rich phase H or  $\delta$ -AlOOH might be the water carrier for the deep interior instead (Ohira et al., 2014). The lithospheric mantle contain 1–2 wt% Al<sub>2</sub>O<sub>3</sub> while the FeO + Fe<sub>2</sub>O<sub>3</sub> content in the lithospheric part is about 8 wt% (Griffin et al., 2009). Thus, the discovery of a new hydrous phase in an iron rich system would be important to consider for the subducting lithospheric mantle particularly after the dehydration of phase H. If the water released from phase H is stored in the  $\eta$  phase, the maximum water content at pressures higher than 54 GPa is probably determined by the water storage capacity of the  $\eta$  phase (which is approximately 2 wt%).

The  $\eta$  phase with a novel channeled structure might be worthwhile to consider for variety of volatiles. The NAL phase with a hollandite-type structure is known to be stable at the  $P$ – $T$  conditions related to the lower mantle (Miura et al., 2000). The NAL phase has three crystallographic sites: one larger site accommodating atoms like Ca and the other two sites accommodating Al or Mg. The channel structure in NAL phase is formed by six AlO<sub>6</sub> octahedra and Ca atoms lie in the channel. The  $\eta$  phase has similar atomic arrangement as the NAL phase, including the channel structure. Our study suggests that the  $\eta$  phase may contain about 2 wt% of water in the channel. While the existence of hydroxyl in the channel of the  $\eta$  phase is likely most logical considering our experimental setup, we cannot rule out the possible existence of other forms of O and H, such as O–O or even H–H, in the channel. The potential existence of these forms is certainly intriguing for the deep mantle geochemistry. Considering that the hollandite-type structure can store some volatiles, such as water and NH<sub>3</sub> (Watenphul et al., 2009; Yang et al., 2017), the  $\eta$  phase with a channeled structure might also be important for the storage of other volatiles in the deep interior.

#### CRediT authorship contribution statement

Huawei Chen and Sang-Heon Shim design the experiments, analyze the data and wrote the manuscript. Sheng-Yi Xie performed DFT calculations. Byeongkwan Ko, Taehyun Kim and Carole Nisr contribute to experiments. Vitali Prakapenka, Eran Greenberg, Dongzhou Zhang, Wenli Bi, Alp E. Ercan, Yongjae Lee contribute to the manuscript.

#### Declaration of competing interest

The authors declare that they have no known competing financial interests or personal relationships that could have appeared to influence the work reported in this paper.

#### Acknowledgements

This work was supported by NSF grants EAR1321976 and EAR1401270 and a NASA grant (80NSSC18K0353) to S.H.S. H.C.

was supported by the Keck Foundation (PI: P. Buseck). Y. L. thanks the Leader Researcher program (NRF-2018R1A3B1052042) of the Korean Ministry of Science and ICT. We thank Kurt Leinenweber and Andrew Chizmeshya for discussions. The results reported herein benefit from collaborations and/or information exchange within NASA's Nexus for Exoplanet System Science (NExSS) research coordination network sponsored by NASA's Science Mission Directorate. The synchrotron experiments were conducted at GSECARS, Advanced Photon Source (APS). GSECARS is supported by NSF-Earth Science (EAR-1128799) and DOE-GeoScience (DE-FG02-94ER14466). APS is supported by DOE, under contracts DE-AC02-06CH11357. The experimental data included in this paper are available by contacting SHDSchim@asu.edu or hchen156@asu.edu.

## Appendix A. Supplementary material

Supplementary material related to this article can be found online at <https://doi.org/10.1016/j.epsl.2020.116551>.

## References

- Blöchl, P.E., 1994. Projector augmented-wave method. *Phys. Rev. B* 50, 17953.
- Bolfan-Casanova, N., Mackwell, S., Keppler, H., McCammon, C., Rubie, D.C., 2002. Pressure dependence of H solubility in magnesio-wüstite up to 25 GPa: implications for the storage of water in the Earth's lower mantle. *Geophys. Res. Lett.* 29, 89–1–89–4. <https://doi.org/10.1029/2001GL014457>.
- Brown, J.M., Shankland, T.J., 1981. Thermodynamic parameters in the Earth as determined from seismic profiles. *Geophys. J. Int.* 66, 579–596. <https://doi.org/10.1111/j.1365-246X.1981.tb04891.x>.
- Bykova, E., Bykov, M., Prakapenka, V., Konôpková, Z., Liermann, H.-P., Dubrovinskaya, N., Dubrovinsky, L., 2013. Novel high pressure monoclinic Fe<sub>2</sub>O<sub>3</sub> polymorph revealed by single-crystal synchrotron X-ray diffraction studies. *High Press. Res.* 33, 534–545.
- Bykova, E., Dubrovinsky, L., Dubrovinskaya, N., Bykov, M., McCammon, C., Ovsyannikov, S., Liermann, H.-P., Kuznetsov, I., Chumakov, A., Rüffer, R., et al., 2016. Structural complexity of simple Fe<sub>2</sub>O<sub>3</sub> at high pressures and temperatures. *Nat. Commun.* 7, 10661.
- Chen, H., Zhou, S., Morgan, D., Prakapenka, V., Greenberg, E., Leinenweber, K., Shim, S.-H., 2019. The O–O bonding and hydrogen storage in the pyrite-type PtO<sub>2</sub>. *Inorg. Chem.* 58, 8300–8307. <https://doi.org/10.1021/acs.inorgchem.9b00046>.
- Dyuzheva, T., Lityagina, L., Nikolaev, N., Martynov, B., Bendeliani, N., 2006. Growth of single crystals of the high-pressure  $\epsilon$ -FeOOH phase. *Crystallogr. Rep.* 51, 342–343.
- Favre-Nicolin, V., Černý, R., 2002. FOX, 'free objects for crystallography': a modular approach to ab initio structure determination from powder diffraction. *J. Appl. Crystallogr.* 35, 734–743.
- Fei, Y., Mao, H., Hemley, R.J., 1993. Thermal expansivity, bulk modulus, and melting curve of H<sub>2</sub>O–ice VII to 20 GPa. *J. Chem. Phys.* 99, 5369–5373.
- Gleason, A., Quiroga, C., Suzuki, A., Pentcheva, R., Mao, W., 2013. Symmetrization driven spin transition in  $\epsilon$ -FeOOH at high pressure. *Earth Planet. Sci. Lett.* 379, 49–55.
- Gleason, A.E., Jeanloz, R., Kunz, M., 2008. Pressure-temperature stability studies of FeOOH using X-ray diffraction. *Am. Mineral.* 93, 1882–1885.
- Griffin, W., O'Reilly, S.Y., Afonso, J.C., Begg, G., 2009. The composition and evolution of lithospheric mantle: a re-evaluation and its tectonic implications. *J. Petrol.* 50, 1185–1204.
- Hirschmann, M.M., 2006. Water, melting, and the deep earth H<sub>2</sub>O cycle. *Annu. Rev. Earth Planet. Sci.* 34, 629–653. <https://doi.org/10.1146/annurev.earth.34.031405.125211>.
- Hohenberg, P., Kohn, W., 1964. Inhomogeneous electron gas. *Phys. Rev.* 136, B864.
- Hu, Q., Kim, D.Y., Liu, J., Meng, Y., Yang, L., Zhang, D., Mao, W.L., Mao, H., 2017. Dehydrogenation of goethite in Earth's deep lower mantle. *Proc. Natl. Acad. Sci. USA* 114, 1498–1501. <https://doi.org/10.1073/pnas.1620644114>.
- Hu, Q., Kim, D.Y., Yang, W., Yang, L., Meng, Y., Zhang, L., Mao, H.-K., 2016. FeO<sub>2</sub> and FeOOH under deep lower-mantle conditions and Earth's oxygen-hydrogen cycles. *Nature* 534, 241–244. <https://doi.org/10.1038/nature18018>.
- Hu, Q., Liu, J., Chen, J., Yan, B., Meng, Y., Prakapenka, V.B., Mao, W.L., Mao, H., 2020. Mineralogy of the deep lower mantle in the presence of H<sub>2</sub>O. *Nat. Sci. Rev.* <https://doi.org/10.1093/nsr/nwaa098>.
- Kohlstedt, D., Keppler, H., Rubie, D., 1996. Solubility of water in the  $\alpha$ ,  $\beta$  and  $\gamma$  phases of (Mg, Fe)<sub>2</sub>SiO<sub>4</sub>. *Contrib. Mineral. Petrol.* 123, 345–357.
- Kohn, W., Sham, L.J., 1965. Self-consistent equations including exchange and correlation effects. *Phys. Rev.* 140, A1133.
- Kresse, G., Furthmüller, J., 1996. Efficient iterative schemes for ab initio total-energy calculations using a plane-wave basis set. *Phys. Rev. B* 54, 11169–11186. <https://doi.org/10.1103/PhysRevB.54.11169>.
- Liu, J., Hu, Q., Kim, D.Y., Wu, Z., Wang, W., Xiao, Y., Chow, P., Meng, Y., Prakapenka, V.B., Mao, H.-K., et al., 2017. Hydrogen-bearing iron peroxide and the origin of ultralow-velocity zones. *Nature* 551, 494.
- Liu, X., Matsukage, K.N., Li, Y., Takahashi, E., Suzuki, T., Xiong, X., 2018. Aqueous fluid connectivity in subducting oceanic crust at the mantle transition zone conditions. *J. Geophys. Res., Solid Earth* 123, 6562–6573.
- Lu, C., Chen, C., 2018. High-pressure evolution of crystal bonding structures and properties of FeOOH. *J. Phys. Chem. Lett.* 9, 2181–2185.
- Mashino, I., Murakami, M., Ohtani, E., 2016. Sound velocities of  $\delta$ -AlOOH up to core-mantle boundary pressures with implications for the seismic anomalies in the deep mantle. *J. Geophys. Res., Solid Earth* 121, 595–609. <https://doi.org/10.1002/2015JB012477>.
- Meng, Y., Liu, X.-W., Huo, C.-F., Guo, W.-P., Cao, D.-B., Peng, Q., Dearden, A., Gonze, X., Yang, Y., Wang, J., et al., 2016. When density functional approximations meet iron oxides. *J. Chem. Theory Comput.* 12, 5132–5144.
- Michael, P.J., 1988. The concentration, behavior and storage of H<sub>2</sub>O in the sub-oceanic upper mantle: implications for mantle metasomatism. *Geochim. Cosmochim. Acta* 52, 555–566. [https://doi.org/10.1016/0016-7037\(88\)90110-X](https://doi.org/10.1016/0016-7037(88)90110-X).
- Miura, H., Hamada, Y., Suzuki, T., Akaogi, M., Miyajima, N., Fujino, K., 2000. Crystal structure of CaMg<sub>2</sub>Al<sub>6</sub>O<sub>12</sub>, a new Al-rich high pressure form. *Am. Mineral.* 85, 1799–1803.
- Murakami, M., Hirose, K., Sata, N., Ohishi, Y., 2005. Post-perovskite phase transition and mineral chemistry in the pyroclitic lowermost mantle. *Geophys. Res. Lett.* 32, L03304. <https://doi.org/10.1029/2004GL021956>.
- Nishi, M., Irifune, T., Gréaux, S., Tange, Y., Higo, Y., 2015. Phase transitions of serpentine in the lower mantle. *Phys. Earth Planet. Inter.* 245, 52–58.
- Nishi, M., Irifune, T., Tsuchiya, J., Tange, Y., Nishihara, Y., Fujino, K., Higo, Y., 2014. Stability of hydrous silicate at high pressures and water transport to the deep lower mantle. *Nat. Geosci.* 7, 224–227. <https://doi.org/10.1038/ngeo2074>.
- Nishi, M., Kuwayama, Y., Tsuchiya, J., Tsuchiya, T., 2017. The pyrite-type high-pressure form of FeOOH. *Nature* 547, 205–208. <https://doi.org/10.1038/nature22823>.
- Nishi, M., Tsuchiya, J., Kuwayama, Y., Arimoto, T., Tange, Y., Higo, Y., Hatakeyama, T., Irifune, T., 2019. Solid solution and compression behavior of hydroxides in the lower mantle. *J. Geophys. Res., Solid Earth* 124, 10231–10239.
- Nishihara, Y., Matsukage, K.N., 2016. Iron-titanium oxyhydroxides as water carriers in the Earth's deep mantle. *Am. Mineral.* 101, 919–927.
- Ohira, I., Ohtani, E., Sakai, T., Miyahara, M., Hirao, N., Ohishi, Y., Nishijima, M., 2014. Stability of a hydrous  $\delta$ -phase, AlOOH–MgSiO<sub>3</sub>(OH)<sub>2</sub>, and a mechanism for water transport into the base of lower mantle. *Earth Planet. Sci. Lett.* 401, 12–17. <https://doi.org/10.1016/j.epsl.2014.05.059>.
- Ohtani, E., Amaike, Y., Kamada, S., Sakamaki, T., Hirao, N., 2014. Stability of hydrous phase H MgSiO<sub>4</sub>H<sub>2</sub> under lower mantle conditions. *Geophys. Res. Lett.* 41, 8283–8287. <https://doi.org/10.1002/2014GL061690>.
- Ono, S., 1998. Stability limits of hydrous minerals in sediment and mid-ocean ridge basalt compositions: implications for water transport in subduction zones. *J. Geophys. Res., Solid Earth* 103, 18253–18267.
- Palatinus, L., Chapuis, G., 2007. SUPERFLIP—a computer program for the solution of crystal structures by charge flipping in arbitrary dimensions. *J. Appl. Crystallogr.* 40, 786–790.
- Palmer, D.C., 2015. Visualization and analysis of crystal structures using Crystal-Maker software. *Z. Kristallogr.* 230, 559–572. <https://doi.org/10.1515/zkri-2015-1869>.
- Pamato, M.G., Myhill, R., Boffa Ballaran, T., Frost, D.J., Heidelbach, F., Miyajima, N., 2015. Lower-mantle water reservoir implied by the extreme stability of a hydrous aluminosilicate. *Nat. Geosci.* 8, 75–79. <https://doi.org/10.1038/ngeo2306>.
- Panero, W.R., Pigott, J.S., Reaman, D.M., Kabbes, J.E., Liu, Z., 2015. Dry (Mg, Fe)SiO<sub>3</sub> perovskite in the Earth's lower mantle. *J. Geophys. Res., Solid Earth* 120. <https://doi.org/10.1002/2014JB011397>.
- Peacock, S.M., 1990. Fluid processes in subduction zones. *Science* 248, 329–337.
- Pearson, D.G., Brenker, F.E., Nestola, F., McNeill, J., Nasdala, L., Hutchison, M.T., Matveev, S., Mather, K., Silversmit, G., Schmitz, S., Vekemans, B., Vincze, L., 2014. Hydrous mantle transition zone indicated by ringwoodite included within diamond. *Nature* 507, 221–224. <https://doi.org/10.1038/nature13080>.
- Perdew, J.P., Burke, K., Ernzerhof, M., 1996. Generalized gradient approximation made simple. *Phys. Rev. Lett.* 77, 3865–3868. <https://doi.org/10.1103/PhysRevLett.77.3865>.
- Prakapenka, V.B., Kubo, A., Kuznetsov, A., Laskin, A., Shkurikhin, O., Dera, P., Rivers, M.L., Sutton, S.R., 2008. Advanced flat top laser heating system for high pressure research at GSECARS: application to the melting behavior of germanium. *High Press. Res.* 28, 225–235. <https://doi.org/10.1080/08957950802050718>.
- Prescher, C., Prakapenka, V.B., 2015. DIOPTAS: a program for reduction of two-dimensional X-ray diffraction data and data exploration. *High Press. Res.* 35, 223–230. <https://doi.org/10.1080/08957959.2015.1059835>.
- Putz, H., Schön, J., Jansen, M., 1999. Combined method for ab initio structure solution from powder diffraction data. *J. Appl. Crystallogr.* 32, 864–870.
- Sano, A., Ohtani, E., Kondo, T., Hirao, N., Kikegawa, T., 2008. Aluminous hydrous mineral  $\delta$ -AlOOH as a carrier of hydrogen into the core-mantle boundary. *Geophys. Res. Lett.* 35, 3303.
- Shim, S.-H., 2017. PeakPo - a python software for X-ray diffraction analysis at high pressure and high temperature. <https://doi.org/10.5281/zenodo.810200>.

- Shim, S.-H., Bengtson, A., Morgan, D., Sturhahn, W., Catalli, K., Zhao, J., Lerche, M., Prakapenka, V., 2009. Electronic and magnetic structures of the postperovskite-type  $\text{Fe}_2\text{O}_3$  and implications for planetary magnetic records and deep interiors. *Proc. Natl. Acad. Sci.* 106, 5508–5512.
- Sturhahn, W., 2000. CONUSS and PHOENIX: evaluation of nuclear resonant scattering data. *Hyperfine Interact.* 125, 149–172.
- Suzuki, A., Ohtani, E., Kamada, T., 2000. A new hydrous phase delta- $\text{AlOOH}$  synthesized at 21 GPa and 1000 C. *Phys. Chem. Miner.* 27, 689–693.
- Toby, B.H., Von Dreele, R.B., 2013. GSAS-II: the genesis of a modern open-source all purpose crystallography software package. *J. Appl. Crystallogr.* 46, 544–549. <https://doi.org/10.1107/S0021889813003531>.
- Watenphul, A., Wunder, B., Heinrich, W., 2009. High-pressure ammonium-bearing silicates: implications for nitrogen and hydrogen storage in the Earth's mantle. *Am. Mineral.* 94, 283–292.
- Weerasinghe, G.L., Pickard, C.J., Needs, R., 2015. Computational searches for iron oxides at high pressures. *J. Phys. Condens. Matter* 27, 455501.
- Wolantin, E., Pruzan, P., Chervin, J., Canny, B., Gauthier, M., Häusermann, D., Hanfland, M., 1997. Equation of state of ice VII up to 106 GPa. *Phys. Rev. B* 56, 5781.
- Yang, Z., Ford, D.C., Park, J.S., Ren, Y., Kim, S., Kim, H., Fister, T.T., Chan, M.K., Thackeray, M.M., 2017. Probing the release and uptake of water in  $\alpha\text{-MnO}_2 \cdot x\text{H}_2\text{O}$ . *Chem. Mater.* 29, 1507–1517.
- Ye, Y., Prakapenka, V., Meng, Y., Shim, S.-H., 2017. Inter-comparison of the gold, platinum, and MgO pressure scales up to 140 GPa and 2,500 K. *J. Geophys. Res., Solid Earth*. <https://doi.org/10.1002/2016JB013811>.
- Yuan, H., Zhang, L., Ohtani, E., Meng, Y., Greenberg, E., Prakapenka, V.B., 2019. Stability of Fe-bearing hydrous phases and element partitioning in the system  $\text{MgO-Al}_2\text{O}_3\text{-Fe}_2\text{O}_3\text{-SiO}_2\text{-H}_2\text{O}$  in Earth's lowermost mantle. *Earth Planet. Sci. Lett.* 524, 115714.
- Zhang, D., Dera, P.K., Eng, P.J., Stubbs, J.E., Zhang, J.S., Prakapenka, V.B., Rivers, M.L., 2017. High pressure single crystal diffraction at PX2. *J. Vis. Exp.*, e54660.